# FINAL REPORT

Finite Element Modeling of Scattering from Underwater Proud and Buried Military Munitions

SERDP Project MR-2408

JULY 2017

Ahmad T. Abawi
**HLS Research**

SERDP
DOD ∙ EPA ∙ DOE

*Page Intentionally Left Blank*

*Page Intentionally Left Blank*

# REPORT DOCUMENTATION PAGE

*Form Approved*
*OMB No. 0704-0188*

| 1. REPORT DATE *(DD-MM-YYYY)* | 2. REPORT TYPE | 3. DATES COVERED *(From - To)* |
|---|---|---|
| 02-28-2017 | Final Report | 03/2014 – 03/2017 |

**4. TITLE AND SUBTITLE**

**5a. CONTRACT NUMBER**

**5b. GRANT NUMBER**

**5c. PROGRAM ELEMENT NUMBER**

**6. AUTHOR(S)**
Ahmad Abawi

**5d. PROJECT NUMBER**

**5e. TASK NUMBER**

**5f. WORK UNIT NUMBER**

**7. PERFORMING ORGANIZATION NAME(S) AND ADDRESS(ES)**

Heat, Light, and Sound Research, Inc.
3366 N Torrey Pines Ct, Suite 310
La Jolla, CA 92037

**8. PERFORMING ORGANIZATION REPORT NUMBER**

**9. SPONSORING / MONITORING AGENCY NAME(S) AND ADDRESS(ES)**
Strategic Environmental Research & Development Program
4800 Mark Center Drive, Suite 17D03
Alexandria, VA 22350

**10. SPONSOR/MONITOR'S ACRONYM(S)**
SERDP

**11. SPONSOR/MONITOR'S REPORT NUMBER(S)**
MR-2408

**12. DISTRIBUTION / AVAILABILITY STATEMENT**

Unlimited

**13. SUPPLEMENTARY NOTES**

**14. ABSTRACT**
The objective of this work has been to develop high fidelity acoustic scattering models that can quickly compute the acoustic color templates (backscattered target strength as a function of frequency and aspect angle) for UXO targets. These models are used to design experiments, interpret collected data and particularly identify features that can be used in classification.

**15. SUBJECT TERMS**

| 16. SECURITY CLASSIFICATION OF: | | | 17. LIMITATION OF ABSTRACT | 18. NUMBER OF PAGES | 19a. NAME OF RESPONSIBLE PERSON Ahmad Abawi |
|---|---|---|---|---|---|
| **a. REPORT** Final | **b. ABSTRACT** U | **c. THIS PAGE** U | U | 41 | **19b. TELEPHONE NUMBER** *(include area code)* 858-457-0800 |

**Standard Form 298 (Rev. 8-98)**
Prescribed by ANSI Std. Z39.18

*Page Intentionally Left Blank*

# SERDP Final Report

# Contents

# List of Figures

## List of Tables

**Abstract**

*Objectives:*   Develop high fidelity acoustic scattering models to facilitate the detection, localization, and characterization of military munitions found in ponds, lakes, rivers, estuaries, and coastal ocean areas. Use these models to design experiments, interpret collected data, identify features that can be used in training classifiers.

*Technical Approach:*   Most acoustic scattering models are well-equipped to compute scattering from elastic objects in free space. However, unexploded ordinance (UXO) reside in complex ocean environments, which have a profound effect on their acoustic response to sonar. Thus, in trying to model the response of UXO to sonar, a high-fidelity model must account for the interaction between the target and its surrounding environment. While the standard method of solution for an arbitrary elastic target is the finite element method, the solution of the scattering problem in the surrounding medium is best handled by the boundary integral equation, as it replaces the infinite domain problem by an integral over the surface of the target. Furthermore, the boundary integral method has the advantage of reducing the dimensionality of the problem by one. In contrast, the finite element method is not well-suited for solving the scattering problem in the surrounding environment due to difficulty in satisfying the radiation condition. For these reasons, we solve the problem of scattering from an elastic target in a complex ocean environment by a combination of finite element method and boundary integral method. We use the finite element method to model the motion of the target by essentially computing its impedance matrix in vacuum, and the boundary integral method to model the acoustic field in its surrounding medium. The two solutions are coupled by satisfying the required boundary conditions on the surface of the target. This results in a model that treats the interaction between the target and its surrounding environment exactly. An important extension of this work is the development of the same model for axially-symmetric targets with substantial speed advantages.

*Results:*  During the past three years, we have been providing benchmark-quality solutions for various targets to researchers within SERDP who do similar type of modeling. While doing this, an important part of our work has been to validate our own models using analytical solutions when available and other well-tested solutions. We validated our 3D and axially-symmetric models in free space using the analytic solution for elastic spheres and spherical shells. We also validated our models for scattering from a proud, half-buried and a fully-buried solid sphere by comparing our results with those of the T-matrix method. We computed the acoustic color (backscattered target strength as function of frequency and angle of incidence) for the aluminum replica of a UXO (henceforth aluminum UXO), the Bullet-105 and the Howitzer shell in free space using both our 3D and axially-symmetric versions of our model. We also computed the acoustic color for the fully proud and the fully buried aluminum UXO and compared our results with measurements and those produced by other models. Additionally, we computed the acoustic color for the partially buried aluminum UXO and again compared our results with other finite element models since measured results for this case was not yet available. The model results in all cases agreed with each other and and with the measurements. To verify that our model indeed accounts for multiple scattering, we computed the acoustic color for a tilted cylinder near the water-air interface and showed that our model results were in total agreement with measurements. Finally, to show that our 3D model is truly 3D and can handle targets of arbitrary shape, we used it to compute the acoustic color for the Bullet-105 UXO with a hole drilled on its side.

*Benefits:* The method that was developed has several advantages over currently-used methods. The most important ones are: 1) The method is inherently broadband since the stiffness and mass matrices, which constitute the impedance matrix, are independent of frequency. Therefore, the computation of these matrices, which makes up the most numerically intensive part of the computation, is performed once for all frequencies. 2) This method is efficient because it requires a matrix inversion for each frequency, but not each angle while computing the acoustic color. This is not the case for currently-used methods, which must solve a full finite element problem for each frequency and each angle of incidence. 3) Since this method computes the target impedance matrix in vacuum, the same impedance matrix can be used in any environment, so changing the environment for the same target does not require a full finite element solution of the problem. 4) By projecting the impedance matrix onto the surface nodes, this method reduces a finite element problem to a boundary element problem with far fewer unknowns. This reduction in the number of unknowns enables the method to solve a 3D problem with ease. 5) It provides a numerically exact solution since it self-consistently couples the target with the surrounding environment. 6) Due its modular nature, the method easily lends itself to parallel processing, including GPU processing and the application of the fast multipole technique.

# Objective

The objective of this work has been to develop high fidelity acoustic scattering models that can quickly compute the acoustic color templates (backscattered target strength as a function of frequency and aspect angle) for UXO targets. These models are used to design experiments, interpret collected data and particularly identify features that can be used in classification.

# Background

Modeling the response of UXOs to a sonar signal in an ocean environment belongs to a large class of problems referred to as the fluid-structure interaction, where the fluid in this case refers to the ocean environment and the structure refers to the UXO. The problem of determining the interaction between a submerged elastic structure and its surrounding fluid is of considerable interest, particularly in underwater acoustics and aeronautics where it is required to determine the acoustic field about an arbitrary three-dimensional structure. While the standard method of solution for an arbitrary elastic structure is the finite element method, the solution of the reduced wave equation in the surrounding medium is best handled by the boundary integral equation, as it replaces the infinite domain problem by an integral over the surface of the submerged structure. Furthermore, the boundary integral method has the advantage of reducing the dimensionality of the problem by one. In contrast, the finite element method is not well-suited for solving the wave equation in the surrounding fluid environment due to difficulty in satisfying the radiation condition as well as demands on the mesh size and the difficulty in generating the fluid mesh.

For these reasons the problem of fluid-structure interaction is perhaps best treated by a combination of finite element method to model the motion of the structure and the boundary integral

method to model the acoustic field in its surrounding medium, where the coupling between the two models is achieved by imposing the continuity of pressure and normal particle velocity at the surface of the structure.

The coupled finite and boundary integral method has been used by several authors in recent years [1]-[10] and (see Amini *et al.* [9] and the references therein). The main differences in these approaches are the particular finite element package and boundary integral formulation employed, the numerical approximation used and the details of the method of coupling.

In this work [10], we use the coupled finite and boundary element methods to compute the scattered acoustic field from an arbitrary elastic structure in an arbitrary medium, characterized by a Green's function. The formulation (also known as the impedance formulation) results in a self-consistent, accurate, and numerically efficient solution that is valid in any environment. In modeling the structure, we use hexahedral eight-node elements to discretize the Galerkin weighted residual equation and in modeling the acoustic environment, we discretize the Helmholtz-Kirchhoff equation by expanding pressure and normal particle velocity in piecewise constant basis functions over quadrilateral elements on the surface of the structure. The finite and boundary element solutions are coupled by imposing the continuity of pressure and normal particle velocity on the surface nodes of the structure. An important part of this work is the development of the coupled finite element/boundary element model for axially-symmetric structures with non-axially-symmetric loading, which reduces the 3D problem to several uncoupled 2D problems, one for each circumferential order of a Fourier expansion.

We refer to the method as the 3D-IMP, (IMP for impedance). The axially-symmetric version of the model is referred to as Axi-IMP.

# Methods

In this section, we will derive the 3D and the axially-symmetric versions of the IMP method, 3D-IMP and Axi-IMP. We will validate the solution for a sphere in free space and two half-space environments. For a sphere in free space we will use its classical partial wave solution as a reference solution and for a sphere in two half-space environment, we will use the T-Matrix [11] as the reference solution.

## The fluid-structure formulation

We use the fluid-structure formulation, based on the work of Wilton, Everstine, Benthien and Schenck [3, 2, 1], where we use the finite element technique to solve the Euler's equation in the elastic target and couple this solution with the solution of the Helmholtz equation in the surrounding medium by using pressure loading as the external force that causes displacements in the elastic target. A more complete derivation of this technique is provided in the above references, but to elucidate the discussions that follow, we summarize the derivation below: We start with the Euler

equation

$$\rho \frac{\partial^2}{\partial t^2} \mathbf{u} + \mathbf{B}^{\mathbf{T}} \mathbf{D} \mathbf{B} \mathbf{u} = \mathbf{F}, \tag{1}$$

Where $\mathbf{u}$ is the displacement vector, $\rho$ is the density, $\mathbf{F}$ is the external force, $\mathbf{B}$ is a rectangular (6x3) differential operator that relates the strain and the displacement and $\mathbf{D}$ is the (6x6) elasticity matrix. The displacement in the elastic target can be expressed in the finite element representation as

$$\mathbf{u}(x) = \sum_{i=1}^{N} u_i \psi_i(x), \quad \mathbf{x} \in R, \tag{2}$$

where $R$ is the region the object occupies, $u_i$ corresponds to the components of the displacement at a finite number of points in the object called nodes, and the function $\psi_i$ forms a three-dimensional basis for piecewise polynomial interpolation between nodes. The finite element equations can be obtained by substituting the expansion (2) in the Euler equation, multiplying it with $\psi_n$ and integrating over the volume to obtain

$$\mathbf{M} \frac{d^2 U}{dt^2} + \mathbf{K} U = F,$$

where

$$M_{mn} = \int \rho \psi_n^T \psi_m dv, \quad K_{mn} = \int \psi_n^T B^T DB \psi_m dv,$$

are respectively the mass and stiffness matrices. If the time dependence is harmonic $(e^{-i\omega t})$ with circular frequency $\omega$, the above equation becomes

$$\left( -\omega^2 \mathbf{M} + \mathbf{K} \right) \mathbf{U} = \mathbf{F}. \tag{3}$$

On the 'wet' surface of the target, the Helmholtz-Kirchhoff integral can be written as

$$\frac{1}{2} p(\mathbf{x}) - \int p(\mathbf{x}') \frac{\partial G(\mathbf{x}, \mathbf{x}')}{\partial n'} ds' = -i\omega\rho \int v(\mathbf{x}') G(\mathbf{x}, \mathbf{x}') ds' + p_{inc}(\mathbf{x}), \quad \mathbf{x} \in S, \tag{4}$$

where $p$ is the pressure, $v$ is the normal particle velocity and $G(\mathbf{x}, \mathbf{x}')$ is the environment Green's function. Expanding $p$ and $v$ in finite element basis functions

$$p(x) = \sum_{i=1}^{N} p_i \phi_i(x), \quad v(x) = \sum_{i=1}^{N} v_i \phi_i(x),$$

and substituting them in (4) gives

$$\mathbf{A} P = \mathbf{B} V + P_{inc}, \tag{5}$$

where

$$A_{mn} = \frac{\delta_{mn}}{2} - \int_{s_n} \frac{\partial G(x_n, x_m)}{\partial n} ds', \quad B_{mn} = -i\omega\rho \int_{s_n} G(x_n, x_m) ds'. \tag{6}$$

4

In the above $\phi_i$ are piecewise-constant basis functions and the integration is performed over surface elements, $s_n$. To couple the elastic and the fluid equations, we note that at the surface node $i$ the force is due to pressure loading

$$F_i = -\int_S p(q)\mathbf{n}_q \cdot \psi_i(q)dS_q.$$

On the other hand

$$p(q) = \sum_{j=1}^{m} p_j \phi_j(q).$$

From these two equations, we obtain

$$F = -\mathbf{L}^T P,$$

where

$$L_{i,j} = \int_S \phi_i(q)\psi_j(q) \cdot \mathbf{n}_q dS_q.$$

The continuity of normal displacement requires that the normal velocity in the fluid should be related to the normal displacement in the structure as

$$V = -i\omega\mathbf{L}\mathbf{u}.$$

Substituting this expression in (3) and (5), we find

$$\mathbf{A}P = -i\omega\mathbf{B}\mathbf{L}\mathbf{u} + P_{inc},$$

$$\left(-\omega^2\mathbf{M} + \mathbf{K}\right)\mathbf{u} = -\mathbf{L}^T P.$$

Eliminating $\mathbf{u}$ in the above two equations gives the pressure

$$P = \left(\mathbf{A} - i\omega\mathbf{B}\mathbf{L}\left(-\omega^2\mathbf{M} + \mathbf{K}\right)^{-1}\mathbf{L}^T\right)^{-1} P_{inc}, \tag{7}$$

and normal particle velocity on the surface

$$V = i\omega\mathbf{L}\left(-\omega^2\mathbf{M} + \mathbf{K}\right)^{-1}\mathbf{L}^T P. \tag{8}$$

Equation (7) relates the total pressure field on the surface of the object to the incident field and a matrix containing information about the surrounding environment in the matrices $\mathbf{A}$ and $\mathbf{B}$ and properties of the elastic object in matrices $\mathbf{L}, \mathbf{M}$, and $\mathbf{K}$. The latter three matrices are computed using a finite element model and the former two and $p_{inc}$ are computed using a propagation model. Once $P$ is computed using (7), (8) is used to compute the normal velocity, $V$. Using the surface pressure and normal velocity, the scattered field, $P^s$, is computed at any arbitrary point using the Helmholtz-Kirchhoff integral

$$P^s = a^T P + b^T V, \quad \text{where} \quad a_n = \int_{S_n} \frac{\partial G(x_r, x')}{\partial n}ds', \quad b_n = i\omega\rho \int_{S_n} G(x_r, x')ds'. \tag{9}$$

5

The most numerically intensive part of computing (7) is computing the inverse of the impedance matrix, $(-\omega^2\mathbf{M}+\mathbf{K})$, since the dimensions of $\mathbf{M}$ and $\mathbf{K}$ are equal to the number of volume elements, which includes interior as well as surface elements. What proved to be a crucial step in this method is the use of modal decomposition to invert the impedance matrix, based on the work of Benthien and Schenck [3]. Introducing the matrix $\mathbf{E}$ whose columns are the normal modes of the structure,

$$\mathbf{KE} = \mathbf{ME}\Omega,$$

where $\Omega$ is the diagonal matrix of *in vacuo* eigenfrequencies of the structure. Since the modes can be normalized so that it is M-orthogonal and K-normalized, we can write

$$\mathbf{E}^T\mathbf{ME} = \mathbf{I}.$$

Then it can be easily verified that

$$\left(-\omega^2\mathbf{M}+\mathbf{K}\right)^{-1} = \mathbf{E}\left(-\omega^2\mathbf{I}+\Omega\right)^{-1}\mathbf{E}^T. \tag{10}$$

Thus, the impedance matrix can be inverted for all frequencies, except those that are the *in vacuo* eigenfrequencies of the structure. If a desired frequency happens to coincide with one of the eigenfrequencies, linear interpolation between neighboring frequencies can be used. Through numerical experimentation we have found that the above result is accurate if the maximum operating frequency is lower than the eigenfrequency of the highest mode. This can simply be accomplished by specifying the number of modes to be computed by the finite element model and making sure that the eigenfrequency of the highest mode is larger than the highest frequency of interest. The use of (7), (8), (10) in (5) completely solves the scattering problem in an environment whose Green's function is specified in (6).

## Modification for axially-symmetric objects in free space

By a process that will be described below, it can be shown that the solution of scattering from an axially-symmetric object with non axially-symmetric loading is equivalent to solving a 3D problem by a series of 2D problems, which results in significant reduction in numerical cost. Referring to Fig. (1) we note that if an axially-symmetric object is insonified by an incident field that is along its axis of symmetry, the field on a line such as $\Lambda$, which is formed by the surface of the object and a plane perpendicular to the axis of symmetry, is constant.
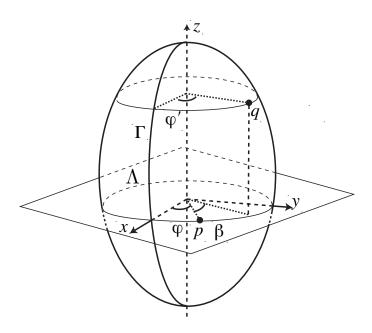
Figure 1: *The geometry of an axially-symmetric object.*

However, if the incident field is not along the axis of symmetry of the object, the field along $\Lambda$ is periodic in azimuthal angle $\phi$. Since this field is only a function of $\phi$, which can only happen for an axially-symmetric object in which case $\Lambda$ is a circle, it can be expanded in an azimuthal Fourier series

$$p(\mathbf{x}) = \sum_{n=0}^{\infty} p_e^n(r,z)\cos(n\phi) + p_o^n(r,z)\sin(n\phi), \tag{11}$$

Since the Fourier coefficients, $p^n$, are not a function of $\phi$, they represent an axially-symmetric load (incident field). Therefore, the above expansion is a sum of axially-symmetric solutions when the loading is not axially-symmetric. If the loading is axially-symmetric, then only the term $n = 0$ contributes. Substituting the above Fourier expansion for the pressure and normal particle velocity into (4) and switching the order of sums and integrals gives

$$\frac{1}{2} \sum_{n=0}^{\infty} \left[ p_e^n(r,z)\cos(n\phi) + p_o^n(r,z)\sin(n\phi) \right]$$

$$- \sum_{n=0}^{\infty} \int \left[ p_e^n(r',z')\cos(n\phi') + p_o^n(r',z')\sin(n\phi') \right] \frac{\partial G(\mathbf{x},\mathbf{x}')}{\partial n'} ds' \tag{12}$$

$$= -i\omega\rho \sum_{n=-\infty}^{\infty} \int \left[ v_e^n(r',z')\cos(n\phi') + v_o^n(r',z')\sin(n\phi') \right] G(\mathbf{x},\mathbf{x}') ds' + p_{inc}(\mathbf{x}).$$

Applying the integral operator

$$\int_0^{2\pi} \cos(\ell\phi)\, d\phi,$$

7

to the above equation results in the boundary element integral equation for the even azimuthal coefficients given by

$$\frac{1}{2}p_e^\ell(r,z) - \int p_e^\ell(r',z')h_e^\ell(r,z;r',z')r'd\Gamma'$$

$$= -i\omega\rho \int v_e^\ell(r',z')g_e^\ell(r,z;r',z')r'd\Gamma' + \frac{p_{inc_e}^\ell(r,z)}{\varepsilon\pi}. \tag{13}$$

where

$$p_{inc_e}^\ell(\mathbf{x}) = \int_0^{2\pi} p_{inc}(\mathbf{x})\cos(\ell\phi)\,d\phi,$$

and

$$g_e^\ell\left(r,z;r',z'\right) = \frac{1}{2\varepsilon\pi}\int_0^{2\pi}\int_0^{2\pi} G(\mathbf{x},\mathbf{x}')\left(\cos\ell(\phi'-\phi)+\cos\ell(\phi'+\phi)\right)d\phi d\phi',$$

$$h_e^\ell\left(r,z;r',z'\right) = \frac{1}{2\varepsilon\pi}\int_0^{2\pi}\int_0^{2\pi} \frac{\partial G(\mathbf{x},\mathbf{x}')}{\partial n'}\left(\cos\ell(\phi'-\phi)+\cos\ell(\phi'+\phi)\right)d\phi d\phi', \tag{14}$$

where $\varepsilon = 2$ for $\ell = 0$ and 1 otherwise. The boundary element equation for the odd azimuthal coefficients is obtained by applying the operator

$$\int_0^{2\pi}\sin(\ell\phi)\,d\phi,$$

to (12). It is given by

$$\frac{1}{2}p_o^\ell(r,z) - \int p_o^\ell(r',z')h_o^\ell(r,z;r',z')r'd\Gamma'$$

$$= -i\omega\rho \int v_o^\ell(r',z')g_o^\ell(r,z;r',z')r'd\Gamma' + \frac{p_{inc_o}^\ell(r,z)}{\pi}, \tag{15}$$

where

$$g_o^\ell\left(r,z;r',z'\right) = \frac{1}{2\pi}\int_0^{2\pi}\int_0^{2\pi} G(\mathbf{x},\mathbf{x}')\left(\cos\ell(\phi'-\phi)-\cos\ell(\phi'+\phi)\right)d\phi\,d\phi',$$

$$h_o^\ell\left(r,z;r',z'\right) = \frac{1}{2\pi}\int_0^{2\pi}\int_0^{2\pi} \frac{\partial G(\mathbf{x},\mathbf{x}')}{\partial n'}\left(\cos\ell(\phi'-\phi)-\cos\ell(\phi'+\phi)\right)d\phi\,d\phi', \tag{16}$$

and

$$p_{inc_o}^\ell(\mathbf{x}) = \int_0^{2\pi} p_{inc}(\mathbf{x})\sin(\ell\phi)\,d\phi.$$

If $G$ is a function of the difference of the angles $(\phi' - \phi)$, as is the case for the free space Green's function, (14) and (16) reduce to

$$g_e^\ell \left(r,z;r',z'\right) = g_o^\ell \left(r,z;r',z'\right) = \int_0^{2\pi} G(\mathbf{x},\mathbf{x}')\cos(\ell\phi')d\phi',$$

$$h_e^\ell \left(r,z;r',z'\right) = h_o^\ell \left(r,z;r',z'\right) = \int_0^{2\pi} \frac{\partial G(\mathbf{x},\mathbf{x}')}{\partial n'}\cos(\ell\phi')d\phi', \tag{17}$$

However, for a general Green's function these equations will be coupled in azimuthal order and require $n^2$ evaluations of the double angular integrals in (14) and (16). In this case, the axially symmetric boundary element formulation has no computational advantage over its 3D counterpart. Discretizing the above equations as was done before and assuming piecewise constant fields, we get for each azimuthal order $\ell$

$$\mathbf{A}^\ell p^\ell = \mathbf{B}^\ell v^\ell + p_{inc}^\ell, \tag{18}$$

where the matrix elements are given by

$$\left(A_{mn}^\ell\right)_{e,o} = \frac{1}{2}\delta_{mn} - \int h_{e,o}^\ell(r_m,z_m;r_n',z_n')r_n'd\Gamma', \tag{19}$$

$$\left(B_{mn}^\ell\right)_{e,o} = -i\omega\rho \int g_{e,o}^\ell(r_m,z_m;r_n',z_n')r_n'd\Gamma', \tag{20}$$

where all variables $(r,z;r',z')$ in (19) and (20) are evaluated on the surface. Note that (18), (19) and (20) are the axially symmetric counterparts of (5) and (6). These equations are valid in the fluid and on the wet surface of the structure. The axially symmetric counterpart of (3) for the structure is given by

$$\left(-\omega^2\mathbf{M}^\ell + \mathbf{K}^\ell\right)\mathbf{U}^l = \mathbf{F}^\ell, \tag{21}$$

where

$$\left(M_{mn}^\ell\right)_{e,o} = \int \rho \; \psi_m^T \; [C_\ell^{e,o}][C_\ell^{e,o}] \; \psi_n \; r'd\Gamma'd\phi',$$

and

$$\left(K_{mn}^\ell\right)_{e,o} = \int \; \psi_m^T \; [C_\ell^{e,o}]B^T DB[C_\ell^{e,o}] \; \psi_n \; r'd\Gamma'd\phi'.$$

The displacement basis functions are given by

$$\psi_m = \begin{bmatrix} \psi_r \\ \psi_z \\ \psi_\theta \end{bmatrix}_m = \sum_{\ell=0}^\infty [C_\ell^e]\begin{bmatrix} \psi_r \\ \psi_z \\ \psi_\theta \end{bmatrix}_{m,\ell}^e + [C_\ell^o]\begin{bmatrix} \psi_r \\ \psi_z \\ \psi_\theta \end{bmatrix}_{m,\ell}^o,$$

9

and

$$[C_\ell^e] = \begin{bmatrix} \cos(\ell\phi) & 0 & 0 \\ 0 & \cos(\ell\phi) & 0 \\ 0 & 0 & -\sin(\ell\phi) \end{bmatrix}, \quad [C_\ell^o] = \begin{bmatrix} \sin(\ell\phi) & 0 & 0 \\ 0 & \sin(\ell\phi) & 0 \\ 0 & 0 & \cos(\ell\phi) \end{bmatrix}.$$

The combination of (18) and (21) results in similar equations as (7) and (8) for the axially symmetric case

$$P_{e,o}^\ell = \left( \mathbf{A}_{e,o}^\ell - i\omega \mathbf{B}_{e,o}^\ell \mathbf{L} \left( -\omega^2 \mathbf{M}_{e,o}^\ell + \mathbf{K}_{e,o}^\ell \right)^{-1} \mathbf{L}^T \right)^{-1} P_{inc_{e,o}}^\ell, \tag{22}$$

and

$$V_{e,o}^\ell = i\omega \mathbf{L} \left( -\omega^2 \mathbf{M}_{e,o}^\ell + \mathbf{K}_{e,o}^\ell \right)^{-1} \mathbf{L}^T P_{e,o}^\ell. \tag{23}$$

Note that for an axially-symmetric problem the sizes of the matrices $\mathbf{M}_{e,o}^\ell$ and $\mathbf{K}_{e,o}^\ell$ are small enough that the matrix inversion

$$\left( -\omega^2 \mathbf{M}_{e,o}^\ell + \mathbf{K}_{e,o}^\ell \right)^{-1},$$

can be performed directly without the use of the modal expansion described by (10).

The integrals in (19) and (20) are performed over the generating curve $\Gamma$. If $\Gamma$ is divided into $N$ linear elements, an integral of the form given in (19) and (20) over a single element $n$ can be written as

$$I_{mn} = \int_{z_n'}^{z_{n+1}'} f^\ell(r_m, z_m; \bar{r}, \bar{z}) \bar{r} \sqrt{1 + \left( \frac{d\bar{r}}{d\bar{z}} \right)^2} \, d\bar{z},$$

where the arc length $d\bar{\Gamma} = \sqrt{1 + (d\bar{r}/d\bar{z})^2}$. Transforming the above integral to a local coordinate system described by

$$\bar{r} = \frac{r_{n+1}' + r_n'}{2} + \frac{r_{n+1}' - r_n'}{2} \xi_n$$
$$\bar{z} = \frac{z_{n+1}' + z_n'}{2} + \frac{z_{n+1}' - z_n'}{2} \xi_n,$$

results in

$$I_{mn}^\ell = \frac{1}{4} \int_{-1}^{1} Q_{mn}^\ell(r_m, z_m; \xi_n) \, d\xi_n, \tag{24}$$

where

$$Q_{mn}^\ell(r_m, z_m; \xi_n) = f^\ell(r_m, z_m; \xi_n) \left( r_{n+1}' + r_n' + \left( r_{n+1}' - r_n' \right) \xi_n \right) \sqrt{\left( r_{n+1}' - r_n' \right)^2 + \left( z_{n+1}' - z_n' \right)^2}.$$

Using two-point Gauss quadrature, the integral in (24) can be evaluated

$$I_{mn}^\ell = Q_{mn}^\ell \left( r_m, z_m; -1/\sqrt{3} \right) + Q_{mn}^\ell \left( r_m, z_m; 1/\sqrt{3} \right).$$

The angular integrals in (17) are evaluated using multi-point Gaussian quadrature.

10

# Validation

Due to its well-known analytic solution, the sphere provides the best method for validating a numerical solution. Here we use a solid steel sphere and an aluminum spherical shell to benchmark Axi-IMP. Figure (2) shows a comparison between the backscattered pressure amplitude from a 0.5 m solid steel sphere computed using Axi-IMP and the classical partial wave solution as a function of frequency.
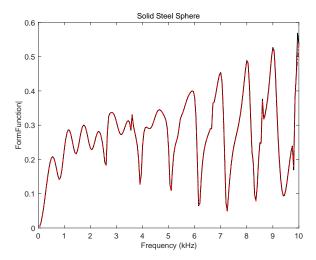


Figure 2: *The scattering amplitude as a function of frequency for a 0.5 m solid steel sphere. The solid line represents the partial wave solution and the red dash-dot line represents the coupled finite-boundary element solution.*

A comparison of the backscattered scattering amplitude computed using Axi-IMP and the partial wave solution for an air-filled aluminum spherical shell is shown in Fig. (3). The radius of the sphere in this case is 0.5 m and the shell thickness is 5 cm. In both cases, there is excellent agreement between our solutions and the benchmark solutions.
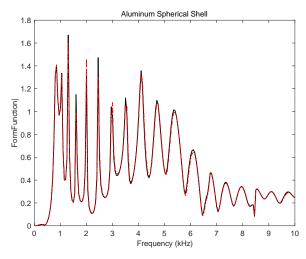


Figure 3: *The scattering amplitude as a function of frequency for a 0.5 m air-filled, aluminum spherical shell. The solid line represents the partial wave solution and the red dash-dot line represents the coupled finite-boundary element solution.*

We validated the 3D version of our model, 3D-IMP, by using spheres in free space and were able to obtain the same excellent agreement with the partial wave solutions as are shown in Figs. (2) and (3). The Green's function used in the above two cases is the free space Green's function given by

$$G\left(\mathbf{x};\mathbf{x}'\right) = \frac{e^{ik\sqrt{(x-x')^2+(y-y')^2+(z-z')^2}}}{4\pi\sqrt{(x-x')^2+(y-y')^2+(z-z')^2}}. \tag{25}$$

Another class of problems with a slightly more complicated Green's function, which also lends itself to an analytical solution is the case of an acoustically soft or rigid hemisphere on an infinite plane satisfying the same boundary conditions. This is also referred to as an infinite plane with a hemispherical boss. The analytical solution is obtained from the partial wave solution using the method of images. The Green's function used in the 3D-IMP formulation for the acoustically soft case with the infinite plane at $z = 0$ is

$$G_D\left(\mathbf{x};\mathbf{x}'\right) = G_1\left(\mathbf{x};\mathbf{x}'\right) - G_2\left(\mathbf{x};\mathbf{x}'\right), \tag{26}$$

where

$$G_1\left(\mathbf{x};\mathbf{x}'\right) = \frac{e^{ik\sqrt{(x-x')^2+(y-y')^2+(z-z')^2}}}{4\pi\sqrt{(x-x')^2+(y-y')^2+(z-z')^2}},$$

$$G_2\left(\mathbf{x};\mathbf{x}'\right) = \frac{e^{ik\sqrt{(x-x')^2+(y-y')^2+(z+z')^2}}}{4\pi\sqrt{(x-x')^2+(y-y')^2+(z+z')^2}}.$$

For the rigid case the Green's function is given by

$$G_N\left(\mathbf{x};\mathbf{x}'\right) = G_1\left(\mathbf{x};\mathbf{x}'\right) + G_2\left(\mathbf{x};\mathbf{x}'\right). \tag{27}$$

These Green's functions guarantee that the total field vanishes on the infinite plane for the acoustically soft case and its normal derivative vanishes on the same surface for the acoustically hard case. The boundary element method then enforces the same boundary conditions on the surface of the hemispherical boss, resulting in a self-consistent solution. In this example, the hemispherical boss has a 0.5 m radius and the problem is solved for a plane wave making a $30°$ angle with the positive $x$-axis for two frequencies of 5 kHz and 10 kHz. The scattered field is computed as a function of the receiver angle. The surface of the hemispherical boss was meshed by approximately 8000 quadrilateral elements. The solutions are shown in Fig. (4), where they are compared with the corresponding exact partial wave solutions.
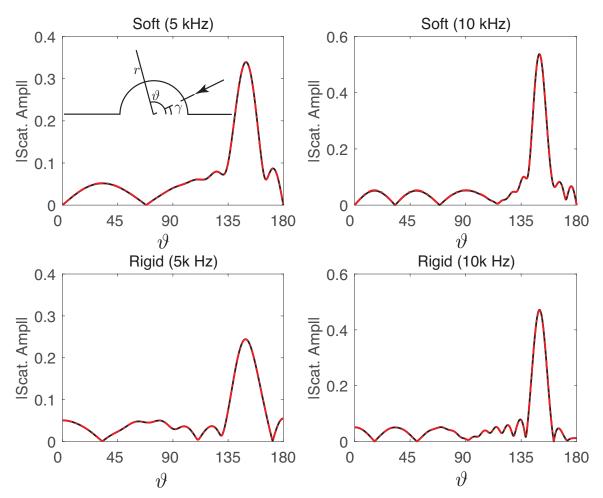
Figure 4: *The scattering amplitude as a function of the receiver angle for a hemispherical boss. The scattering geometry is shown in the inset in the top left panel. The incident plane wave makes an angle $\gamma = 30°$ with the x-axis in all cases. The receiver angle, $\vartheta$ varies from zero to $180°$. The top and bottom panels show the results for the acoustically soft and rigid cases, respectively. The left and right panels are for the incident frequency of 5 kHz and 10 kHz. The solid lines are for the exact partial wave solutions and the broken red lines are for coupled 3D-IMP solution.*

The next order of complexity arises when the ocean environment is composed of two fluid half spaces: a water half space over a fluid bottom half space. In most practical cases the ocean environment is modeled this way, so it is appropriate to validate this solution for this type of environment. Since the T-Matrix solution is designed for spherical targets, in this validation process we will use a solid sphere. We will consider three cases, fully proud, fully buried and partially buried. As will be seen, the latter case proves to be quite challenging.

If the waveguide is composed of a water half-space with sound speed $c_1$ and density $\rho_1$ over a bottom half-space with sound speed $c_2$, density $\rho_2$, and interface at $z = 0$, the Green's function is given by

$$G(r,z;r_s,z_s) = \int_0^\infty \tilde{G}(k_r,z;z_s)J_0(k_r|r-r_s|)k_r dk_r, \tag{28}$$

13

where $r_s$ and $z_s$ are the source range and depth and $r$ and $z$ are the receiver range and depth, $J_0$ is the Bessel function of order zero and the spectral Green's function $\tilde{G}(k_r, z; z_s)$ for a source located in the water is given by

$$\tilde{G}(k_r, z; z_s) = \begin{cases} \dfrac{iRe^{ik_{z_1}(z+z_s)}}{4\pi k_{z_1}} + \dfrac{ie^{ik_{z_1}|z-z_s|}}{4\pi k_{z_1}} & \text{for} \quad z \geq 0, \\[4mm] \dfrac{iTe^{ik_{z_1}z_s}e^{-ik_{z_2}z}}{4\pi k_{z_1}} & \text{for} \quad z < 0, \end{cases} \tag{29}$$

where $k_{z_1} = \sqrt{k_1^2 - k_r^2}$, $k_{z_2} = \sqrt{k_2^2 - k_r^2}$, $\omega$ is the circular frequency and the reflection and transmission coefficients are given by

$$R = \frac{k_{z_1}\rho_2 - k_{z_2}\rho_1}{k_{z_1}\rho_2 + k_{z_2}\rho_1}, \quad T = \frac{2k_{z_1}\rho_2}{k_{z_1}\rho_2 + k_{z_2}\rho_1}, \quad k_i = \frac{\omega}{c_i}, \ i = 1, 2.$$

The above Green's functions are used to compute the incident field, the matrices $\mathbf{A}$ and $\mathbf{B}$, given in (6) and the scattered field given in (9). The matrices $\mathbf{A}$ and $\mathbf{B}$ represent the interaction between surface elements, where one element plays the role of the source and the other the role of the receiver in (29) and (30). Similarly, in computing the scattered field, the surface elements play the role of the sources. For this reason, if the entire target or any part of it is in the bottom half space, we need a spectral Green's function for a source in the bottom, which is given by

$$\tilde{G}(k_r, z; z_s) = \begin{cases} \dfrac{iTe^{ik_{z_1}z}e^{-ik_{z_2}z_s}}{4\pi k_{z_2}} & \text{for} \quad z \geq 0, \\[4mm] \dfrac{-iRe^{-ik_{z_2}(z+z_s)}}{4\pi k_{z_2}} + \dfrac{ie^{ik_{z_2}|z-z_s|}}{4\pi k_{z_2}} & \text{for} \quad z < 0, \end{cases} \tag{30}$$

where now the reflection and transmission coefficients are given by

$$R = -\frac{k_{z_1}\rho_2 - k_{z_2}\rho_1}{k_{z_1}\rho_2 + k_{z_2}\rho_1}, \quad T = \frac{2k_{z_2}\rho_1}{k_{z_1}\rho_2 + k_{z_2}\rho_1}.$$

By substituting (29) and (30) in (28), we obtain for the source in the water

$$G(r, z; r_s, z_s) = \begin{cases} \displaystyle\int_0^\infty \dfrac{iRe^{ik_{z_1}(z+z_s)}}{4\pi k_{z_1}} J_0(k_r|r-r_s|)k_r dk_r + g_w(k_1, r, z; r_s, z_s) & \text{for} \quad z \geq 0, \\[5mm] \displaystyle\int_0^\infty \dfrac{iTe^{ik_{z_1}z_s}e^{-ik_{z_2}z}}{4\pi k_{z_1}} J_0(k_r|r-r_s|)k_r dk_r & \text{for} \quad z < 0, \end{cases} \tag{31}$$

and for the source in the bottom

$$G(r, z; r_s, z_s) = \begin{cases} \displaystyle\int_0^\infty \dfrac{iTe^{ik_{z_1}z}e^{-ik_{z_2}z_s}}{4\pi k_{z_2}} J_0(k_r|r-r_s|)k_r dk_r & \text{for} \quad z \geq 0, \\[5mm] \displaystyle\int_0^\infty \dfrac{-iRe^{-ik_{z_2}(z+z_s)}}{4\pi k_{z_2}} J_0(k_r|r-r_s|)k_r dk_r + g_w(k_2, r, z; r_s, z_s) & \text{for} \quad z < 0, \end{cases} \tag{32}$$

14

where

$$g_w(k,r,z;r_s,z_s) = \frac{e^{ik\sqrt{(r-r_s)^2+(z-z_s)^2}}}{4\pi\sqrt{(r-r_s)^2+(z-z_s)^2}},$$

is the free space Green's function, which represents the direct wave[1] and can also be represented by the Sommerfeld-Wyle integral in the spectral domain

$$g_w(k,r,z;r_s,z_s) = \frac{i}{4\pi} \int_0^\infty \frac{e^{ik_z|z-z_s|}}{k_z} J_0(k_r|r-r_s|)k_r dk_r. \tag{33}$$

The computation of matrices $\mathbf{A}$ and $\mathbf{B}$ requires $n^2$ evaluations of the Green's functions, where $n$ is the number of surface elements. For a typical target, we have anywhere between 6 to 20 thousand surface elements, which means that the computation of these matrices requires on the order of one hundred million function evaluations. This becomes a daunting numerical task when the Green's functions are represented in terms of spectral integrals as in (31) and (32). For a target located entirely in the water, the Green's function is given by the top equation in (31) and for one located entirely in the bottom it is given by the bottom equation in (32). We note that in these two cases the Green's functions are a function of the sum of source and receiver depths, $(z+z_s)$, and the difference of their ranges, $|r-r_s|$. So in these two cases, the Green's functions are a function of two parameters as opposed to four $(r,z;r_s,z_s)$, which allows for the use of 2D interpolation. For the cases of fully proud and fully buried targets, we computed the Green's functions on a $200 \times 200$ grid as a function of the sum of source and receiver depths and the difference of their ranges around the target, and computed their values at the surface elements using two-parameter interpolation. This essentially reduced the number of function evaluations from $10^8$ to $10^4$ and proved to be a crucial step in our ability to compute the acoustic color for targets of interest. Figure (5) shows the interaction between surface elements and their corresponding Green's functions. For the case of a partially buried target, the situation is more complicated. Referring to Fig. (5), in this case the Green's functions are a function of source depth, $z_s$, receiver depth, $z$, and the difference between their ranges, $|r-r_s|$, which would require a 3-parameter interpolation. Three-parameter interpolation is also numerically expensive and does not provide a computational advantage. To deal with this situation, we divide the interaction matrix ($\mathbf{A}$ or $\mathbf{B}$) into four sub-matrices, depending on the locations of sources and receivers. This is shown by the cartoon in Fig. (6). We compute sub-matrices 1 and 4 by using interpolation as we did for the cases of fully proud and fully buried targets, respectively. This is also shown in the top two panels of Fig. (5). We compute sub-matrix 2 directly and sub-matrix 3 from sub-matrix 2 by applying a special form of reciprocity according to the equations

$$g_3(k_r,z,z_s) = \frac{\rho_1}{\rho_2} g_2(k_r,z,z_s)^T,$$

$$\frac{dg_3(k_r,z,z_s)}{dx} = -\frac{\rho_1}{\rho_2} \left( \frac{dg_2(k_r,z,z_s)}{dx} \right)^T,$$

$$\frac{dg_3(k_r,z,z_s)}{dy} = -\frac{\rho_1}{\rho_2} \left( \frac{dg_2(k_r,z,z_s)}{dy} \right)^T,$$

$$\frac{dg_3(k_r,z,z_s)}{dz} = -ik_{z_2} \frac{\rho_1}{\rho_2} \left( \frac{dg_2(k_r,z,z_s)}{dz} \right)^T,$$

---

[1]The direct wave is a wave that does not interact with the boundaries of the waveguide.

$$G(r, z; r_s, z_s) = \int_0^\infty \frac{iRe^{ik_{z_1}Z}}{4\pi k_{z_1}} J_0(k_r|R|)k_r dk_r + \text{Direct Field},$$



$$Z \equiv z_s + z_r, \quad R \equiv r_s - r_r, \quad k_{z_i} = \sqrt{k_i^2 - k_r^2},$$

$$G(r, z; r_s, z_s) = \int_0^\infty \frac{-iRe^{-ik_{z_2}Z}}{4\pi k_{z_2}} J_0(k_r|R|)k_r dk_r + \text{Direct Field},$$



$$G(r, z; r_s, z_s) = \begin{cases} \int_0^\infty J_0(k_r|r - r_s|) \dfrac{iTe^{ik_{z_1}z}e^{-ik_{z_2}z_s}}{4\pi k_{z_2}} k_r dk_r, & \text{for} \quad z \geq 0, \ z_s < 0 \\ \\ \int_0^\infty J_0(k_r|r - r_s|) \dfrac{iTe^{ik_{z_1}z_s}e^{-ik_{z_2}z}}{4\pi k_{z_1}} k_r dk_r, & \text{for} \quad z < 0, \ z_s \geq 0 \end{cases}$$



Figure 5: *The interaction between surface elements and their corresponding Green's functions for a fully proud, fully buried and partially buried target.*

where $g_2$ is the spectral Green's function for sub-matrix 2, $g_3$ is the same for sub-matrix 3 and the superscript $T$ indicates matrix transpose. So in doing this, we have reduced the computation from $O((\ell + m)^2)$ to approximately $O(m\ell)$, where $\ell \times m$ is the size of sub-matrix 2. This gave us the ability to compute scattering from a partially buried target in a reasonable time.

Figure 6: *The interaction matrix is divided into four sub-matrices depending on the locations of sources and receivers.*

To validate our solution, we computed scattering from a fully proud, fully buried and partially buried solid sphere and compared our results to those obtained by the T-Matrix method. The T-Matrix method is a semi-analytic formulation [12], based on the analytic solution of the wave equation for a sphere. For this reason, it produces almost exact solutions for spherical objects. We used a version of the T-Matrix method that is designed to compute scattering from a sphere in a multi-layer environment [11]. In this simulation, the sphere is made of tungsten carbide with a radius of 6.35 mm. The environment consisted of a water half space on top of a fluid bottom half space. The water sound speed is 1485.4 $m/s$ with a density of 1000 $kg/m^3$, and the bottom sound speed and density are 1655 $m/s$ and 1890 $kg/m^3$, respectively. We computed the backscattered scattering amplitude as a function of $ka$ for a proud, buried and half buried sphere at a backscattered angle of 50°, measured in the counterclockwise direction from the interface, where $k = \omega/c_1$ and $a$ is the radius of the sphere. The scattering geometry for each case is shown in the cartoon in the left panel of each figure, where the arrows only indicate the angle of incidence and scattering, but *do not* represent the ray paths. This is an exact model and includes all multi-paths. In Fig. (7) we show a comparison of our result with that of the T-Matrix solution for a fully proud sphere.
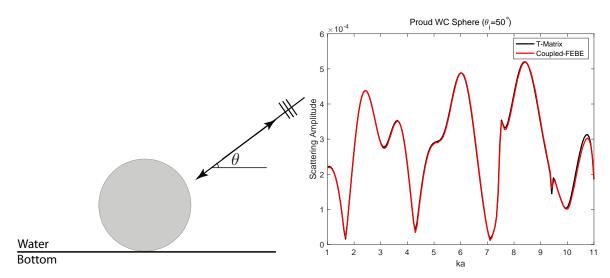
Figure 7: *Comparison of backscattered scattering amplitude as a function of ka for a solid, proud tungsten carbide sphere computed using the T-Matrix method (black line) and the 3D-IMP method. The scattering geometry is shown in the figure on the left. The incident field is a plane wave and θ = 50°. The receiver is at one meter from the center of the sphere in the direction of the incident field.*

The scattering amplitude as a function of *ka* for the same sphere buried in the bottom such that its center is 8 mm below the interface is compared with the T-Matrix solution in Fig. (8).



Figure 8: *Comparison of backscattered scattering amplitude as a function of ka for a buried tungsten carbide sphere computed using the T-Matrix method (black line) and the 3D-IMP method. The scattering geometry is shown in the figure on the left, where θ = 50° and the receiver is at one meter from the center of the sphere in the direction of the incident field.*

The scattering amplitude as a function of *ka* for the same sphere, half buried is compared with the T-Matrix solution in Fig. (9).
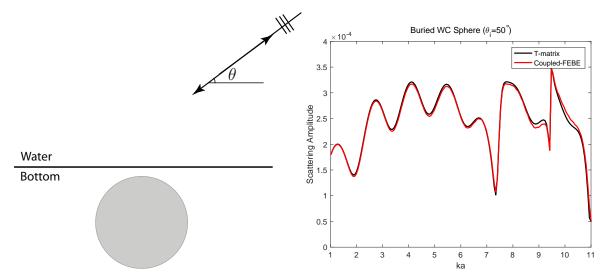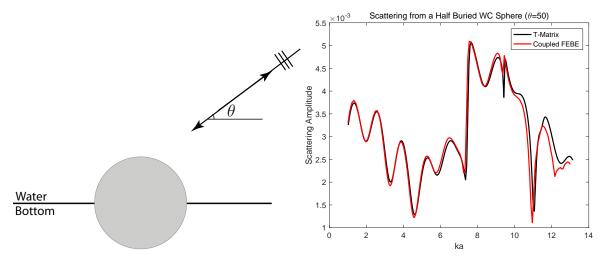
18

Figure 9: *Comparison of backscattered scattering amplitude as a function of ka for a half buried tungsten carbide sphere computed using the T-Matrix method (black line) and the 3D-IMP method. The scattering geometry is shown in the figure on the left, where θ = 50° and the receiver is at one meter from the center of the sphere in the direction of the incident field.*

The agreement between the two models in all the above cases is excellent. The minor differences between the two models, particularly in the case of the half-buried sphere, are hard to explain since both models are susceptible to numerical error and the partially buried case is also more challenging to the T-Matrix method. Errors at higher frequencies could also be because we use fewer elements than necessary. Increasing the number elements increases computational time and dealing with it is an issue that we plan to address in the future.

## The advantages of the IMP method

Most problems of interest to SERP are numerically too demanding to be solved on a regular desktop computer by conventional finite element model that treats the target as 3D and includes the environment as part of the computational domain. The development of the model AxiScat [13] was an effort to reduce computational complexity. This model, which is in use by some investigators working for SERDP computes scattering from an axially-symmetric target in free space for a given incident plane wave. Its limitations are that the target must be axially-symmetric and the environment that embeds it must be free space. But in most simulations involving UXOs, the environment is modeled by two half-spaces. The presence of the interface causes singly and multiply-reflected rays to also ensonify the target. To approximate the solution in this environment using AxiScat, scattering due to these rays is computed individually and added to the scattering that is caused by the direct ray. This is an approximate solution since in solving the scattering problem, it is always assumed that the target is in free space and the effects of the interface is added later, which ignores coupling effects. This solution is referred to as the Hybrid solution since it uses a combination of finite elements and ray theory to solve the problem. In contrast, our solution is numerically exact since the environment is integrated into the solution through the environment Green's function and it can be any environment. For this reason, part of our collaborative work with other SERDP researches has been to provide benchmark solutions. Other advantages of the method are listed below:

1. The most important advantage of the IMP technique is its speed and efficiency in computing the scattered field for a range of frequencies. While the Hybrid method solves the scattering problem for every frequency, the IMP method uses the finite element technique to compute the matrices **C**, **M**, **K**, **D** and **E** in vacuum independent of frequency and uses (7) to compute the scattered field for any desired frequency. This technique is much more efficient in computing the acoustic color.

2. The other advantage of the IMP technique, which is enormously useful in computing acoustic color plots, is that it only requires matrix inversion for every frequency, but not for every angle. This is because in (7) the incident field, which contains the angle information appears on the right-hand side. In contrast, since the Hybrid method solves a finite element problem for every frequency and every incident angle, it requires matrix inversion at every frequency and angle.

3. The IMP technique completely decouples the surrounding environment, represented by matrices **A** and **B** from the elastic target represented by matrices, **C**, **M**, **K**, **D** and **E**. Once these matrices are computed in vacuum, they can be used in any environment. One can therefore construct a library of impedance matrices for all targets of interest and compute scattering from them in any desired environment. Furthermore, by solving the finite element problem in vacuum, there is no need to use PMLs or similar techniques to impose the radiation condition. These techniques are often tricky and seldom unreliable.

4. The IMP technique self-consistently couples the target with the surrounding environment and provides a numerically exact solution of the problem regardless of whether the target is in free space, a multi-layered medium or a waveguide. Most conventional finite element techniques, on the other hand, compute scattering in a small computational domain around the target and can only treat the presence of boundaries outside of this domain using a single-scatter approximation, which ignores multiple scattering. As is shown in the next section, this solution becomes highly inaccurate when these boundaries are close to the target, but not close enough to be included in the computational domain.

5. Due its modular nature, the IMP technique lends itself to the use of parallel processing, including GPU processing and fast multipole method (FMM) [14]-[18] to substantially improve its speed even further.

## Results and Discussions

In this section, we validate the axially-symmetric and 3D versions of our method, Axi-IMP and 3D-IMP using analytical solutions when possible, and semi-analytic solutions based on the T-Matrix method. The use of analytic solutions as benchmark solutions is motivated by the desire to demonstrate the accuracy of our method without having to worry about the accuracy of the benchmark solution. Obviously, analytical solutions are numerically exact and even though the T-Matrix solution in only semi-analytic, it is the next best solution, particularly for a sphere. After the models are validated, we apply them to compute the acoustic color for various UXOs and compare results with measurements.

## Applications

### Axi-IMP

We applied the axially symmetric formulation (Axi-IMP) to compute the acoustic color templates for a variety of targets and compared the execution times between this technique, the 3D-IMP and the axially symmetric finite element solution, AxiScat. Figure (10) shows the results for an aluminum replica of a UXO, whose length is approximately 48 cm and its maximum diameter is about 10 cm. The aspect angle is measured from the tip the UXO, where angles 0, 90 and 180 degrees correspond to tip-on, broadside and end-on incidence, respectively. The top left panel was obtained by the axially symmetric finite element model, AxiScat, and it took 40 hours. The top right figure was obtained by the Axi-IMP and it only took 3 hours for 10 azimuthal orders. The same computation was carried out by 3D-IMP (not shown) and that took 24 hours. There is a rule of thumb for determining the minimum number of azimuthal orders needed for a solution to converge. For targets similar in size and the range of frequencies shown here, this number is on the order of 20. However, we used azimuthal orders that were less than 20 and the solutions seem to have converged.
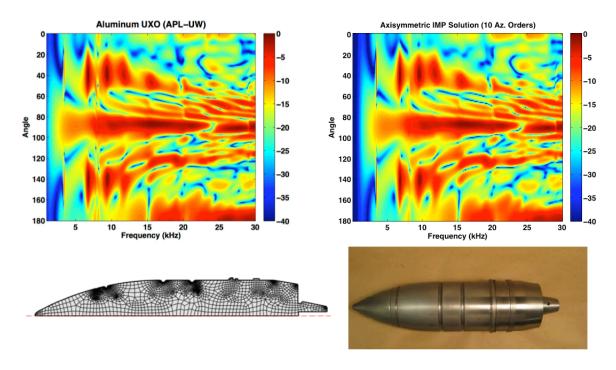


Figure 10: *The acoustic color template for the aluminum UXO replica. The top left panel was obtained using AxiScat and it took 40 hours. The top right panel was obtained using Axi-IMP and it took only 3 hours for 10 azimuthal orders. The bottom left panel shows the 2D quadrilateral mesh on the cross section of the UXO, which is revolved around the axis of symmetry to obtain the 3D object. The bottom right panel is a picture of the target.*

The acoustic color templates for another UXO referred to as Bullet 105 are shown in Fig. (11). The aspect angle in this simulation is measured from broadside, where -90 degrees corresponds

21

to tip-on incidence and 90 degrees corresponds to end-on incidence. The length of this target is slightly under 50 cm and its maximum exterior diameter is approximately 11 cm. It is made of three materials, aluminum, steel and copper. In the bottom right panel of Fig. (11) the shape of the Bullet 105 is depicted, where red, gray and light red represents copper, steel and aluminum, respectively. It also has a cavity inside that in this simulation was assumed to be filled with air. The axially symmetric finite element computation for this target using AxiScat, shown in the top left panel, was carried out by APL-UW, so we are not sure how long it took, but our computation using the Axi-IMP, shown in the top right panel, only took 3.8 hours for 16 azimuthal orders and based on the results shown in Fig. (10), we can safely assume that our solution is at least 10 times faster [2].
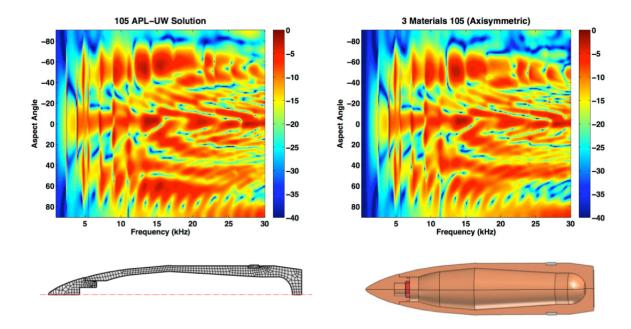


Figure 11: *The acoustic color template for Bullet-105. The top left panel was obtained using Ax-iScat . The top right panel was obtained using AxiSym-IMP and it took 3.8 hours for 16 azimuthal orders. The bottom left panel shows the 2D quadrilateral mesh on the cross section of the target, which is revolved around the axis of symmetry to obtain the 3D object. The bottom right panel shows a depiction of the target.*

We next computed the acoustic color template for the Howitzer UXO. This is a complex target made of five materials, steel, mild steel, copper, plastic and aluminum. This target is about 85 cm long and its maximum radius is about 10 cm. In our simulations we assumed that the target was filled with air. The acoustic color template took 9.5 hours to compute using 16 azimuthal orders. The results are shown in Fig. (12).

---

[2]We compared the execution times between AxiScat and Axi-IMP by computing the acoustic color for a $1 \times 2$ foot aluminum cylinder from 0 to 10 kHz and from 0 to 90 degrees on a Mac Pro. AxiScat took 8 hours, while Axi-IMP took only 19 minutes.
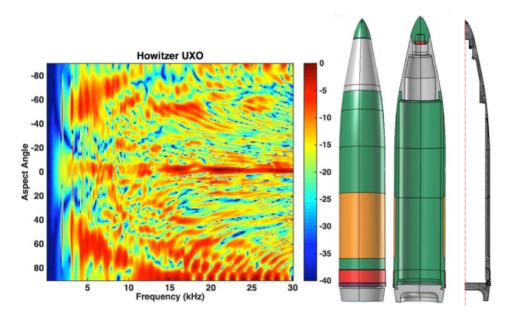
Figure 12: *The acoustic color template for the Howitzer UXO. The tip-on incidence is at -90 degrees and the end-on incidence is at 90 degrees. The figure on the far right shows the finite element mesh used in this computation. The computation took 9.5 hours for 16 azimuthal orders.*

The above run times for the models used are summarized in the table below. Note that 'N/A' in the table indicates that we have no data on the corresponding models/targets, but based on the other results, rough estimates of run times can be assessed. Note also that even though solution in free space is listed as a limitation for both AxiScat and Axi-IMP, solution in a waveguide can be obtained by adding multi-paths in post processing. This is done in the AxiScat examples shown in this report (see Figs. 14-16) and can also be done using the Axi-IMP solution. But these solutions are approximate and not self-consistent since the finite element solution for each multi-path assumes that the target is in free space. The 3D-IMP solution does not have any of these limitations.

| | AxiScat | Axi-IMP | 3D-IMP |
|---|---|---|---|
| Aluminum Cylinder | 8 hours | 19 minutes | 1.5 hours |
| Aluminum UXO | 40 hours | 3 hours | 24 hours |
| Bullet-105 | N/A | 3.8 hours | 32 hours |
| Howitzer UXO | N/A | 9.5 hours | 85 hours |
| Limitations | Axi-symmetric/Free Space | Axi-symmetric/Free Space | None |

Table 1: *Comparison of run times between different models. Note that the run times for the aluminum cylinder are for 100 frequencies between 1-10 kHz. For the other targets they are for 300 frequencies between 1-30 kHz. Also note that the run times for the 3D-IMP model is competitive with the other two models despite the fact that it does not take advantage of the axially-symmetric nature of the target, as do the other two models. 'N/A' indicates that no data are available for the corresponding models/targets.*

## 3D-IMP

We pointed out earlier that despite its amazing speed, the Axi-IMP model can only be applied to axially-symmetric targets in free space. For general-shaped targets or even for axially-symmetric targets in an environment other than free space, we must use the 3D version of the model, 3D-IMP. In what follows we apply this model to simulate various experimental scenarios. One such scenario is depicted by Fig. (13), which describes the experimental setup involving an aluminum replica of a proud UXO used in one of the PondEx experiments off the coast of Panama City, Florida.
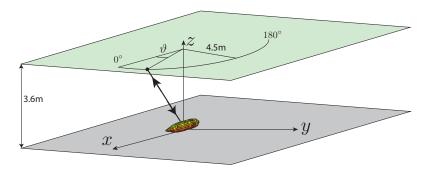


Figure 13: *The PondEx experiment involving scattering from a proud UXO.*

In this experiment, the target is proud on the bottom and the source and receiver trace a semi-circle of 4.5 m radius around the target at a plane 3.6 m from the bottom. In this setup zero and 180 degrees corresponded to tip-on and end-on incidence. In our simulation, we modeled the ocean environment as two fluid half spaces. The model values for the bottom density and sound speed were 2000 kg/m$^3$ and 1694 m/s, respectively. The acoustic color is shown in Fig. (14), where the left panel shows the experimental results, the middle panel our results and the right panel results obtained by APL-UW. We see that the two modeled results agree very well and they agree reasonably well with the experimental results.
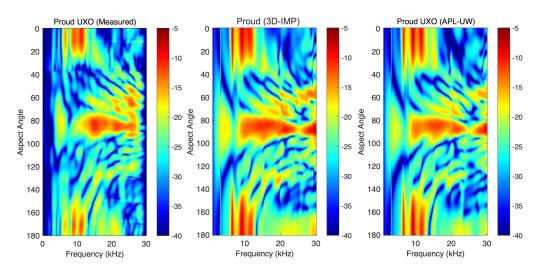


Figure 14: *The acoustic color results for the proud aluminum UXO. The left panel shows experimental results, the middle computed using our 3D model, 3D-IMP, and the right panel shows computed results from APL-UW using their Hybrid method.*

Similar results for a buried UXO with otherwise identical experimental geometry are shown in Fig. (15). The target is buried in such a way that its axis of symmetry is parallel to the water/bottom interface and its top is approximately 5 cm below the interface. Again there is good agreement between the two models and reasonable agreement with the measured results.
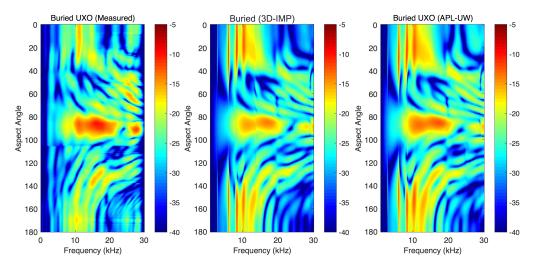


Figure 15: *The acoustic color results for the buried aluminum UXO. The left panel shows experimental results, the middle computed using our 3D model, 3D-IMP, and the right panel shows computed results from APL-UW using their Hybrid method.*

The acoustic color for a half buried UXO is shown in Fig. (16), where in this case the source/receiver geometry is the same, except the UXO is buried in such a way that its axis of symmetry is parallel to and at the same level as the interface. Unfortunately, we were not able to obtain measured results for this case, so we compare our modeled results with those of APL-UW's Hybrid technique. It should be pointed out that the small differences between our results and those of APL-UW may be because our solution is numerically exact and thus includes multiple scattering to all orders, where those of APL-UW accounts for only four principal rays.

In examining the acoustic color for the aluminum replica of a UXO shown in Fig. (10) we notice the presence of three resonances around 3, 6 and 9 kHz and aspect angles of 40 and 140 degrees. These resonances are due to the first three bending modes of the UXO. The first bending mode is a high Q mode that occurs around 3 kHz. The reason these resonances occur at the above angles is that the UXO radiates most efficiently at these angles. Simulations show that this seems to be the characteristic of all objects of this size with a circular cross section. Examining the acoustic color for the same UXO in a two half-space environment in Figs. (14), (15) and (16) shows the existence of the same resonances, but with angles shifted towards tip-on and endfire directions by the presence of the interface. However, these resonances seem to be robust features that can be used for classification.
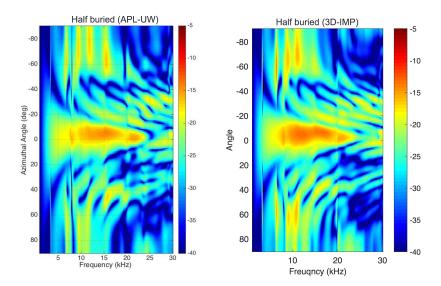
25

Figure 16: *The acoustic color results for the half buried aluminum UXO. The left panel shows computed results using our 3D model, 3D-IMP, and the right panel shows those from APL-UW using their Hybrid method.*

Since the computation of matrices **A** and **B** for the exact Green's functions given by (31) and (32) is numerically very intensive, it has been common practice to approximate these Green's functions by free space Green's functions. This is called the single-scatter approximation. We pointed out before that if the Green's functions do not satisfy the waveguide boundary conditions, an exact solution cannot be obtained, and among other things, the solution will not be able to account for multiple scattering. To experimentally test the accuracy of the single-scatter approximation, an experiment was carried out at Washington State University.

In the experiment the details of which are given in [19], an aluminum cylinder (*length* $= 50.8$ *mm*, *radius* $= 12.7$ *mm*) was suspended from two strings (not shown) attached to the top and bottom of the cylinder. The lengths the strings could vary, thereby allowing the tilt angle of the cylinder to vary. The strings were attached to a circular platform above the water, which could be turned, thus allowing the cylinder to be rotated in a horizontal plane. The transducer was stationary in the water, producing an incident field that made a $19.5°$ angle with the water surface. By rotating the cylinder, the incident angle could be varied, exposing the cylinder to the incident field in a full angular range of $180°$. In the scenario shown in the figure, the lengths of the strings are adjusted in such a way that the side attached to one string is exactly at air-water interface and the axis of the cylinder makes a $34°$ angle with the surface of the water. In our simulations, instead of rotating the cylinder, we rotated the source as is shown in Fig. (17).
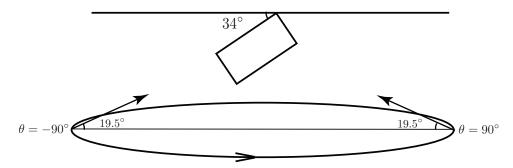
26

Figure 17: *The tilted cylinder experiment geometry.*

In this geometry, when the source is at $\theta = 90°$ the incident field is multiply scattered by the cylinder and the water surface. This is shown in Fig. (18)
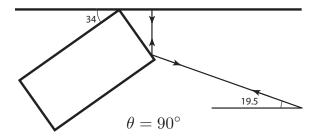


Figure 18: *Multiple scattering by the cylinder and the water surface.*

The measured acoustic color plot for the tilted cylinder is shown in Fig. (19), where the strong response due to the multiply-scattered ray can be seen at $\theta = 90°$ for $ka \gtrsim 6.5$.
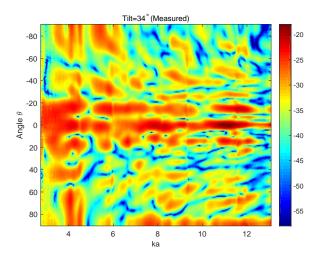


Figure 19: *The measured acoustic color as a function of ka and angle $\theta$ (see Fig. (17)). The strong response due to the multiply-scattered ray can be seen at $\theta = 90°$ and $ka \gtrsim 6.5$.*

Since the pressure is zero at the water surface $(z = 0)$, the Green's function satisfying the boundary condition at the surface can be obtained from the method of images

$$G\left(x,y,z;x',y',z'\right) = \frac{1}{4\pi}\left\{G_- - G_+\right\}, \tag{34}$$

27

where

$$G_-\left(x,y,z;x',y',z'\right) = \frac{e^{ik\sqrt{(x-x')^2+(y-y')^2+(z-z')^2}}}{\sqrt{(x-x')^2+(y-y')^2+(z-z')^2}},$$

and

$$G_+\left(x,y,z;x',y',z'\right) = \frac{e^{ik\sqrt{(x-x')^2+(y-y')^2+(z+z')^2}}}{\sqrt{(x-x')^2+(y-y')^2+(z+z')^2}}.$$

The acoustic color computed using our model, which uses the correct Green's function given by (34) and the single-scatter model, which uses a free space Green's function (the first term in (34)) are shown in Fig. (20).



Figure 20: *The acoustic color for the tilted cylinder computed using our 3D-IMP model on the left and a model that uses the single-scatter approximation on the right. The strong response due to the multiply-scattered ray can be seen at $\theta = 90°$ and $ka \gtrsim 6.5$ in the 3D-IMP solution, but it is absent in the single-scatter solution.*
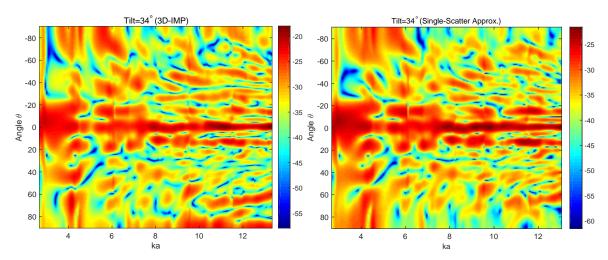
This figure shows that the strong response due to the multiply-scattered ray at $\theta = 90°$ is present in the result on the left, which uses the correct Green's function, and is absent in the single-scatter solution. This proves that to be able account for multiple scattering, the single-scatter approximation is not adequate and one should use the proper Green's functions, i.e. those that satisfy the environment boundary conditions.

As a final example that involves the use of both Axi-IMP and 3D-IMP models, we computed the acoustic color for the Bullet-105 UXO with a hole drilled onto its side. This allows water to enter the UXO, which will affect its acoustic response. Further, from a computational point of view, the presence of the hole breaks the axial symmetry of the target and the problem can no longer be solved by an axially-symmetric model. So we used our 3D model, 3D-IMP. With the computational advantages that 3D-IMP has, it was able to solve this problem in 70 hours on an Apple Mac Pro. With a conventional finite element method it is impossible to solve this problem on a regular desktop computer. The results are shown in Fig. (21). The figure on the left shows the

3D-IMP solution for the UXO with a hole, and for comparison, the figure on the right shows the acoustic color for the same UXO without the hole, which we obtained using our axially-symmetric model, Axi-IMP. This solution only took 3.8 hours to run, which shows once more the computational advantage of the axially-symmetric model, when it can be employed. The bottom two figures show CAD illustrations of the UXO with and without the hole. It is important to note that the presence of the hole changes the acoustic color significantly.
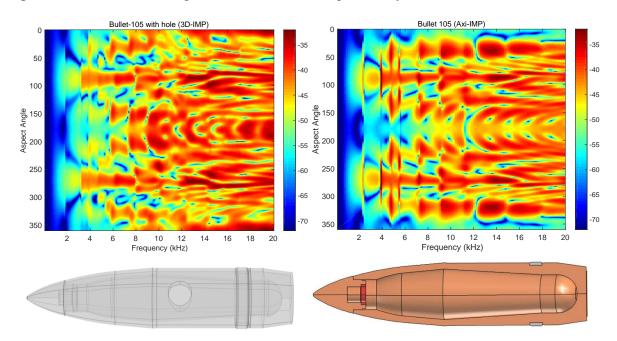


Figure 21: *The acoustic color for a the Bullet-105 UXO with a hole drilled on its side on the left and the same solution for the UXO without the hole. The angle 0 corresponds to tip-on, 90 to broadside and 180 to end-on incidence. The bottom two figures show CAD illustrations of the UXO with and without the hole.*

# Summary and Conclusions

During the last three years, we developed numerical tools to compute scattering from an arbitrary elastic target in an arbitrary ocean environment. These models are based on the fluid-structure interaction method, which uses the finite element method to compute the impedance matrix for the target and the boundary element method to compute the propagation in the environment in which the target is embedded. The two solutions are coupled by imposing the continuity of the pressure and normal particle velocity on the surface of the target. This method produces a system of equations that is self-consistent and rigorously integrates propagation and scattering. This means that it produces a numerically exact solution for scattering from an elastic target in any ocean environment that can be characterized by a Green's function.

We also developed an axially-symmetric version of the model, which we refer to as the Axi-IMP. This model can be applied to an axially-symmetric target for an arbitrary (not necessarily axially-symmetric) incident field in free space. Since most of the targets of interest are axially-symmetric,

29

this model proves to be very useful. It was shown in this report that scattering from an axially-symmetric target in a two half-space environment can be solved by using a combination of ray theory to determine which rays, in addition to the incident ray, are incident on the target, and the AxiScat model to compute the scattered field for each ray. The problem can then be solved as a superposition of the solution for each ray. Even though this is not an exact solution, it is very accurate, as was shown in Figs. (14), (15) and (16). Our axially-symmetric model, Axi-IMP, can do these types of computations at much faster speeds (see the footnote on page 21).

We validated both models by computing the backscattered field from a sphere in free space and compared our results with those obtained from the classical partial wave solution of the sphere. We also validated the 3D-IMP by computing backscattering from a proud, partially buried and fully buried sphere and compared our results with those of the T-Matrix method. Once the models were validated, we computed the acoustic color for various UXOs in free space and from an aluminum replica of a UXO that was used in the PondEx experiments. In the latter case, we compared our results to measurements and showed that the our models matched experimental results pretty well and contained most of the features seen in the measured results. We also demonstrated that the 3D-IMP correctly accounted for multiple scattering, as advertised, by computing the acoustic color for a $1 \times 2$ inch aluminum cylinder near the air-water interface and comparing our results with measurement. These measurements were made in a carefully designed experiment at Washington State University to look for the effects of multiple scattering. Finally, we applied the 3D-IMP to compute scattering from a UXO with a hole drilled on its side. Even though the UXO is axially-symmetric, the presence of the hole breaks this symmetry and the problem can only be solved by a 3D model. We compared the acoustic color for this case with that without the hole and showed that the presence of the hole significantly changes the acoustic color, not particularly because of the presence of the hole, but because the UXO is flooded. This is the type of simulation that would be needed to study the effects of long-term exposure to the harsh ocean environment on the acoustic response of the UXOs.

Even though the 3D-IMP can compute the acoustic color for all UXOs of interest in reasonable times, the execution times can be reduced drastically by the use of modern techniques like the fast multipole method (FMM) [14]-[18] and hierarchical matrices (H-Matrices) [20] and [21]. One reason that the current execution times are manageable is that problems are meshed at the lowest levels possible. For example, the rule of thumb is that one should have on the order 15 elements per wavelength for an accurate solution, but lack of memory and CPU force this number to be on the order 6-10. The use of the above-mentioned techniques reduces most operations that are on the order $O(n^2)$ to $O(n \times log(n))$, where $n$ is the number of elements. This is achieved by rigorously maintaining a pre-specified error tolerance. With type of reduction in execution, one can be more generous with the number of elements and thus also increase the accuracy of the solution. We plan to implement these techniques in our models in the future.

# References

[1] D. T. Wilton, "Acoustic radiation and scattering from elastic structures," International Journal for Numerical Methods in Engineering **13**, 123–138 (1978).

[2] G. C. Everstine and F. M. Henderson, "Coupled finite element/boundary element approach for fluid-structure interaction," J. Acoust. Soc. Am. **87 (5)**, 1938–1947 (1990).

[3] G. W. Benthien and H. A. Schenck, "Structural-acoustic coupling," in *Boundary element methods in acoustics*, edited by R. D. Ciskowski and C. A. Brebbia (Springer, New York, 1977), pp. 109–128.

[4] A. T. Abawi, "The fluid-structure interaction technique specialized to axially symmetric targets," J. Acoust. Soc. Am. **136**, 2086 (2014).

[5] A. T. Abawi, "The use of the virtual source technique in computing scattering from periodic ocean surface," J. Acoust. Soc. Am. **130(2)**, 683 (2011).

[6] A. T. Abawi, "Low frequency scattering from elastic objects embedded in a waveguide by the finite element technique," J. Acoust. Soc. Am. **129**, 2684 (2011).

[7] A. T. Abawi, "Scattering from elastic objects in a waveguide by the finite element technique," J. Acoust. Soc. Am. **128**, 2292 (2010).

[8] A. T. Abawi and M. B. Porter, "Exact and approximate methods for scattering from targets embedded in a layered medium," J. Acoust. Soc. Am. **125**, 2731 (2009).

[9] S. Amini, P. J. Harris, and D. T. Wilton, in *Coupled Boundary and Finite Element Methods for the Solution of the Dynamic Fluid-Structure Interaction Problem* (Springer-Verlag, New York, 1992), Chap. 2 and 4.

[10] A. T. Abawi and P. Krysl, "Coupled finite/boundary element formulation of scattering from elastic objects in a layered medium," J. Acoust. Soc. Am., (2016), to be resubmitted after revison.

[11] R. Lim, "Acoustic scattering by a partially buried three-dimensional elastic obstacle," J. Acoust. Soc. Am. **104(2)**, 769–782 (1998).

[12] P. C. Waterman, "Matrix theory of elastic wave scattering," J. Acoust. Soc. Am. **60**, 567–580 (1976).

[13] M. Zampolli, A. Tesei, F. B. Jensen, N. Malm, and J. B. Blottman, "A computationally efficient finite element model with perfectly matched layers applied to scattering from axially symmetric objects," J. Acoust. Soc. Am. **122**, 1472–1485 (2007).

[14] L. Greengard and V. Rokhlin, "A fast algorithm for particle simulations," Journal of Computational Physics **135**, 280–292 (1997).

[15] V. Rokhlin, "Rapid solution of integral equations of classical potential theory," Journal of Computational Physics **60**, 187–207 (1985).

[16] L. Greengard, *The Rapid Evaluation of Potential Fields in Particle Systems* (MIT Press, Cambridge, MA, 1988).

[17] E. Darve, "The fast multipole method: Numerical implementation," Journal of Computational Physics **160**, 195–240 (2000).

[18] N. Nishimura, "Fast multipole accelerated boundary integral equation methods," App. Mech. **55(4)**, 299–324 (2002).

[19] K. W. Daniel Plotnick, Philip Marston and A. España, "High frequency backscattering by a solid cylinder with axis tilted relative to a nearby horizontal surface," J. Acoust. Soc. Am. **137 (1)**, 470–480 (2015).

[20] S. Börm, L. Grasedyck, and W. Hackbusch, "Introduction to hierarchical matrices with applications," Engineering Analysis with Boundary Elements **27**(5), 405–422 (2003).

[21] S. Börm, L. Grasedyck, and W. Hackbusch, "Hierarchical matrices," Lecture notes **21**, 2003 (2003).